Indentation modulus at the macro-scale level measured by Brinell and Vickers indenters by using the primary hardness standard machine at INRiM

ACTA IMEKO
ISSN: 2221-870X
March 2019, Volume 8, Number 1, 3-12

Indentation modulus at the macro-scale level measured by Brinell and Vickers indenters by using the primary hardness standard machine at INRiM

Alessandro Schiavi[1], Claudio Origlia[1], Alessandro Germak[1], Giulio Barbato[2], Giovanni Maizza[3], Gianfranco Genta[2], Roberto Cagliero[3], Gianluca Coppola[1,2]

[1] INRIM – National Institute of Metrological Research, Str.delle Cacce 91, 10135 Torino, Italy
[2] Politecnico di Torino DIGEP, C.so Duca degli Abruzzi 24, 10129 Torino, Italy
[3] Politecnico di Torino DISAT, C.so Duca degli Abruzzi 24, 10129 Torino, Italy

ABSTRACT
In this paper, the experimental procedure and calculation model for the measurement of the indentation modulus by using the primary hardness standard machine at INRiM in the macro-scale range at room temperature is described. The indentation modulus is calculated based on the Doerner-Nix linear model and from accurate measurements of indentation load, displacement, contact stiffness, and hardness indentation imaging. Measurements are performed with both pyramidal (Vickers test) and spherical indenters (Brinell test). Test force is provided by a dead-weight machine, and the occurring displacement is measured by a laser-interferometric system. The geometrical dimensions of both the Vickers and Brinell indentations are measured by means of a micro-mechanical system and optical microscopy imaging techniques. Applied force and indentation depth are measured simultaneously, at a 16 Hz sampling rate, and the resultant loading-unloading indentation curve is obtained. Preliminary tests are performed on metal and alloy samples. Considerations and comments on the accuracy of the proposed method and analysis are discussed.

Section: RESEARCH PAPER

Keywords: Hardness; indentation modulus; macro-scale

Citation: Alessandro Schiavi, Claudio Origlia, Alessandro Germak, Giulio Barbato, Giovanni Maizza, Gianfranco Genta, Roberto Cagliero, Gianluca Coppola, Indentation modulus at the macro-scale level measured by Brinell and Vickers indenters by using the primary hardness standard machine at INRiM, Acta IMEKO, vol. 8, no. 1, article 2, March 2019, identifier: IMEKO-ACTA-08(2019)-01-02

Editor: Petri Koponen, MIKES Metrology, Finland

Received July 31, 2018; **In final form** January 31, 2019; **Published** March 2019

Funding: This work was supported by EURAMET - EMPIR project 14IND03 “Strength-ABLE”.

Corresponding author: Alessandro Schiavi, e-mail: a.schiavi@inrim.it

1. INTRODUCTION

The elastic properties of materials in mechanical engineering and material science can be evaluated by means of several different experimental techniques that are based on static, quasi-static, and dynamic methods. These techniques involve, for example, measurements of tensile or compressive stress strain, resonance methods, and NDT-based methods, such as measurements of acoustic wave propagation speed in solids or phonon detection. Moreover, techniques involving instrumented indentation (from the nano to the macro scale) that are used to evaluate the elastic properties of materials and procedures are embodied in ISO 14577-1 [1] (for metallic materials). As it is known, the elastic response of materials may vary as a function of the different experimental techniques, measurement procedures, and other boundary conditions used. Consequently, the relevant differences in Young’s modulus values can be easily achieved. In the case of instrumented indentation, ISO selected the specific name of “indentation modulus” and the symbol E_{IT} for underlining possible differences. From a metrological point of view, “hardness” is actually the only quantity (although conventionally defined) collected in the Calibration and Measurement Capabilities (CMC) of the BIPM and supported by international key comparisons. Consequently, the possibility of evaluating the elastic properties from consolidated and accurate experimental procedures is a promising attempt to reduce some sources of uncertainty and dispersion in experimental results.

Observation of elastic recovery effects in indentation tests dates back to 1961, specifically the study of Stilwell and Tabor

[2]. The first attempts to measure hardness and elastic modulus by instrumented indentation were made in 1983 by Pethicai, Hutchings, and Oliver, investigating a method of evaluating hardness at a nano-scale level. Their findings showed that depth-sensing indentation allows the construction of a load-displacement curve, which is strongly related to the typical stress-strain diagrams of materials [3]. In 1986, Doerner and Nix improved the existing methods by using a high-resolution depth-sensing instrument [4]. In 1992, Oliver and Pharr introduced a practical model for measuring hardness and elastic modulus by instrumented indentation [5]. At present, these models are included in ISO 14577; nevertheless, several important changes have been proposed during past decades, improving both the accuracy and application field of the models [6]-[11].

In this paper, the elastic properties of copper alloy, aluminum alloy, brass and stainless steel samples are investigated in terms of the indentation modulus using the macro-indentation test. Measurements are performed using the primary hardness dead weight machine, designed and realized at INRiM.

2. INDENTATION MODULUS

The method for measuring the indentation modulus by means of the indentation technique was introduced by Oliver and Pharr in 1992 [5]. The indentation modulus, E_{IT}, is properly the elastic response of a material when subjected to the action of a concentrated load in a single point. Occurring deformations are not linear; consequently, indentation modulus represents a reasonably close estimation of Young's modulus, in particular, at the macro-scale level. Indentation modulus E_{IT} depends on several parameters and boundary conditions, and it is expressed as:

$$E_{IT} = \frac{1-\nu_s^2}{\frac{2\sqrt{A_p}}{S\sqrt{\pi}} - \frac{1-\nu_i^2}{E_i}} \quad (1)$$

where ν_s is the Poisson ratio of tested material; ν_i and E_i are the Poisson ratio and the Young's modulus of the indenter material respectively; S is contact stiffness, i.e., the incremental ratio between unloading force and related displacement at the maximum depth of indentation; and A_p is the projected contact area, i.e., the value of the indenter area function at the contact depth.

The contact stiffness S is experimentally determined from the best fit of the unloading indentation curve, as the incremental ratio $S = \partial F / \partial h|_{hMAX}$.

The projected contact area A_p depends on the depth h_c of the contact of the indenter with the sample at F_{MAX} and on the type of indenter.

For the Vickers diamond pyramidal indenter, with a vertex angle α, the projected contact area is determined by:

$$A_p = \left(2h_c \cdot \tan\frac{\alpha}{2}\right)^2 \quad (2)$$

and the Brinell tungsten carbide spherical indenter, with a radius R, can be determined by:

$$A_p = \pi h_c \cdot (2R - h_c) \quad (3)$$

In both cases, the depth h_c of the contact of the indenter with the sample at F_{MAX} is determined as a function of frame compliance C_f as follows:

$$h_c = h_{MAX} - \varepsilon \cdot \frac{F_{MAX}}{S} - C_f \cdot F_{MAX} \quad (4)$$

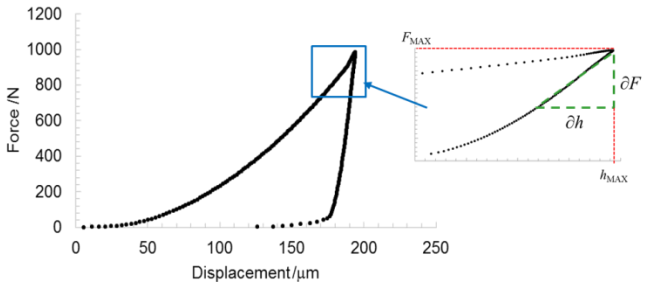

Figure 1. Loading-unloading indentation curve, as a function of applied force and displacement, with an indication of the quantities used in the model.

in which h_{MAX} is the maximum indentation depth; F_{MAX} is the maximum applied force; ε is a value depending on the indenter geometry and the extent of plastic yield in the contact (for both Vickers and Brinell $\varepsilon = 0.75$); S is the contact stiffness; and C_f is the frame compliance.

Once the maximum applied force F_{MAX} and the maximum depth of indentation h_{MAX} are known, indentation modulus E_{IT} can be calculated by using the indentation geometrical dimensions (in particular, the length of the two diagonals and radius) from Vickers and Brinell's experimental data and from the slope of the indentation curve (during the unloading path). In particular, an accurate evaluation of contact stiffness S depends on the best fit of the unloading path. In Figure 1, an experimental loading-unloading indentation curve, as a function of true applied force and displacement, is shown.

ISO 14577-1 recommends two methods of fitting the curve: by means of a linear model (Doerner-Nix method), taking into account the initial 20 % of the unloading curve, and by a power-law model (Oliver-Pharr method), taking into account a range between 50 % and 80 % of the unloading curve. In the linear model, it is assumed that the first portion of the unloading curve is linear and only the linear portion to intercept the displacement axis is extrapolated. The power-law model relies on the depth of the unloading point, which has a high uncertainty both in terms of its measurement and the last part of elastic recovery; therefore, in this paper, only the linear model is used in order to fit the unloading curve.

3. EVALUATION OF FRAME COMPLIANCE

Frame compliance C_f is an experimental quantity that takes into account the whole deformation occurring in the testing machine during the indentation test. Frame compliance affects the accuracy of the indentation modulus measurement [10] as well as the elasto-plastic deformations occurring in the sample under investigation. The elasto-plastic behavior of the materials is investigated from the evaluation of piling-up and sinking-in effects on the resulting hardness indentations. In order to estimate the actual frame compliance, in this paper, two methods are compared: the first according to ISO 14577-1, based on a series of loading and unloading cycles, the second according to the existent literature [11], [12], based on the actual indentation depth of the Vickers and/or Brinell indentation.

In general terms, frame compliance C_f can be considered as the difference between the total compliance C_{tot} and the sample compliance C_s [13] as follows:

$$C_f = C_{tot} - C_s = \left.\frac{\partial h}{\partial F}\right|_{F=F_{MAX}} - \frac{\sqrt{A_p}}{S}\frac{\sqrt{H_{IT}}}{F_{MAX}} \quad (5)$$

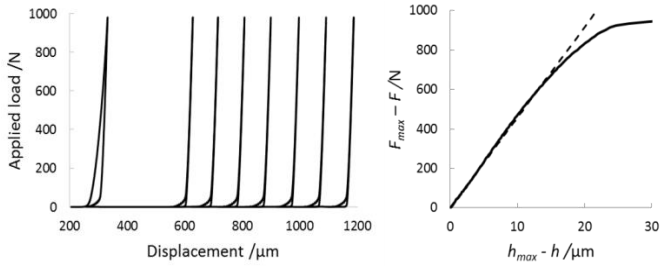

Figure 2. Series of loading-unloading cycles on a single point and linear regression of the last reversed unloading curve.

in which total compliance C_{tot} is determined as the reciprocal of contact stiffness, measured after a series of loading and unloading cycles on a single point, and sample compliance C_s depends on indentation hardness H_{IT}, on contact stiffness S, and on projected contact area A_p of the Vickers or Brinell indenters.

The frame compliance is determined after several cycles of loading and unloading until the slope of the unloading curve is constant, according to the Standard [1], on a stainless steel sample, as shown in Figure 2. The reciprocal of contact stiffness, as shown in equation (5), allows for calculating the value of the frame compliance. In this study, $C_f = 22.1 \times 10^9$ m/N.

Frame compliance C_f is also calculated based on indentation depth (determined from the actual indentation geometry) and the maximum indentation depth (measured during the test).

Assuming that, for many metallic materials, the elastic recovery upon unloading induces a very small elastic deformation at the corners of a Vickers indentation, between the loaded and unloaded condition, a negligible change in the diagonal dimensions is therefore expected [13]. An estimation of the frame compliance is as follows:

$$C_f = \frac{\Delta h}{F_{MAX}} = \frac{h_{MAX} - h_v}{F_{MAX}} \tag{6}$$

in which Δh is determined from the difference between the indentation depth reached during the indentation test h_{MAX} and the indentation depth h_v derived from the resulting indentation geometry.

A similar approach is also proposed for the Brinell indentation; nevertheless, in this case, a relevant change in the radius dimension is expected. In fact, pile-up and sink-in effects influence the radius calculation as well, and they must be taken into account. In Figure 3, typical Vickers and Brinell hardness indentations are shown.

Diagonal lengths of a Vickers pyramidal indentation and the diameter of a Brinell spherical indentation are measured with an accuracy of 0.1 µm. A micro-mechanical system and an optical microscopy imaging technique (INRIM patent) are used for measurement of the indentation geometry.

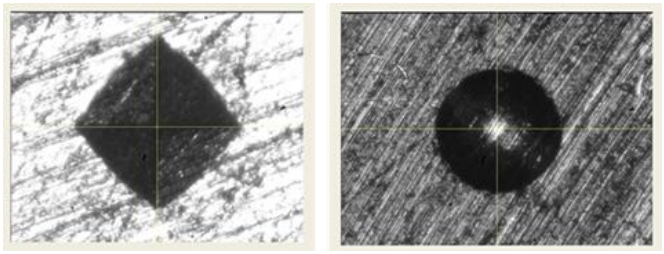

Figure 3. Microscopic image of a typical pyramid indentation of a Vickers hardness test and a spherical indentation of a Brinell hardness test, on a metallic surface.

3.1. Frame compliance from the Vickers indentation

In order to evaluate the frame compliance from the Vickers indentation by means of equation (6), it is necessary to accurately evaluate the resultant indentation depth h_v from the geometrical dimensions of the indentation. In particular, by measuring the length of indentation sides l, indentation depth h_v is given by:

$$h_v = \frac{l}{2} \cdot \cot\frac{\alpha}{2} \tag{7}$$

where the square-based diamond pyramid indenter that is actually used has a measured vertex angle of $\alpha = 135.9°$ between opposite faces, and the side indentation length l is calculated from the two diagonal ds, since a greater accuracy can be achieved,

$$l = \frac{d_1 + d_2}{2} \cdot \sin\frac{\pi}{4}, \tag{8}$$

where d_1 and d_2 are the two measured diagonals of the Vickers indentation.

3.2. Frame compliance from the Brinell indentation

It is also possible to determine the frame compliance from the Brinell indentation. In this case, the indentation depth h_v depends on the radius R of the spherical indenter used and on the radius r of the resulting indentation, as follows:

$$h_v = R - \sqrt{R^2 - r^2} \tag{9}$$

For spherical indentation, the material around the contact area can be deformed upwards (piling up) or downwards (sinking in) along the axis to which load is applied [14]. Indeed, such surface deformation modes influence the measurements of hardness and the indentation modulus, as the true contact area between the indenter and the specimen increases in the case that piling up predominates and decreases in the event that sinking in predominates [15]. The following relationship links the contact area and the indenter displacement measured during the continuous indentation test:

$$c^2 = \frac{r^2}{2 h_v R} \tag{10}$$

In this equation, c^2 quantifies the degree of piling up and sinking in during the indentation test, $c^2 > 1$ indicates piling up, and $c^2 < 1$ accounts for sinking in. In general terms, it is expected that if $c^2 \approx 1$, the surface deformations can be considered negligible and the frame compliance can consequently be determined on the basis of the proposed equation (6).

In the graph shown in Figure 4, the distribution of

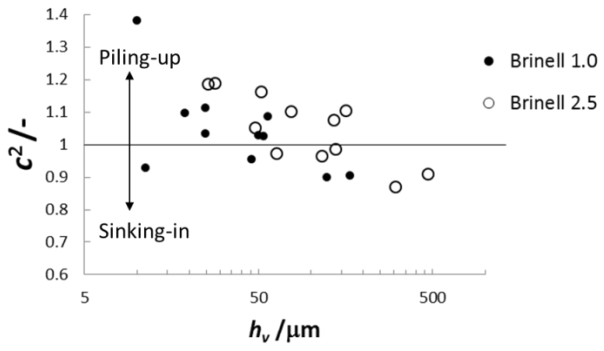

Figure 4: Experimental data on the c^2 parameter as a function of indentation depth, evaluated by the Brinell test with indenter diameters of 1.0 mm and 2.5 mm.

parameter ι^2 as a function of indentation depth h_v, for all tested materials, is shown. The experimental data values are shown in Table 6, Table 7, Table 8, and Table 9.

For each single measurement, it is clear that it is possible to evaluate the degree of the piling up and sinking in that is occurring. In particular, sinking-in effects increase as a function of increasing indentation depth.

3.3. Experimental evaluation of frame compliance

The data on frame compliance C_f calculated by means of equation (6) from the shapes of both the Vickers pyramidal indentations and the Brinell spherical indentations and from the maximum applied force, ranging from ~10^{-10} m/N to ~10^{-7} m/N, as shown in Tables 2-9. Data in brackets (referred to as HV3) are considered outliers. It is clear that both the Vickers and Brinell methods return a coherent dispersion of the frame compliance values as a function of the applied force; in particular, the effects of frame compliance are relevant to the low values of applied force. The proposed method allows us to accurately quantify the actual frame compliance for each single measurement, taking into account the whole deformation occurring during the indentation test as a function of maximum indentation depth.

Average values, calculated by equation (5), $C_f \approx 0.022$ μm/N and by equation (6) $C_f \approx 0.031$ μm/N, can be considered as in agreement. In the graph shown in Figure 5, a comparison between the standard method and the proposed method is shown.

4. PRIMARY HARDNESS STANDARD MACHINE

Measurements of indentation modulus are performed by using the INRiM Primary Hardness Standard dead weight machine, shown in Figure 6. The Standard machine at INRiM was realized in the early 1970s and improvements have continued to be made to it until the present day. Its technical features and metrological characterization are summarized in detail in [16]-[18]. The system generates force by moving a series of dead weights, and a laser interferometric system is used for indentation depth measurements. Test forces are generated by dead weights and are measured along the scale by a force transducer; experimental values are determined with an accuracy range of 0.01 %. The laser beam is aligned on the measurement axis, and experimental values are determined with a resolution of 0.02 μm. Force and indentation depth are monitored in real time, and dates are recorded with a sampling rate of 16 Hz.

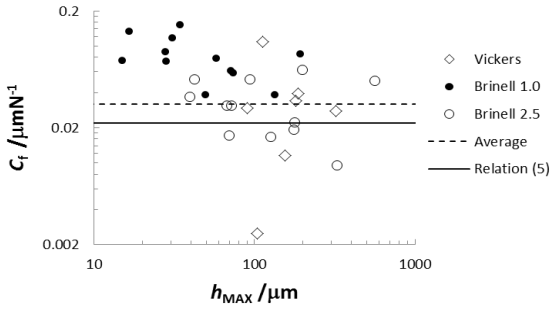

Figure 5: Comparison between frame compliances calculated by equation (5), continuous line and single values from Vickers and Brinell measurements, determined by equation (6). The dotted line is the average value of frame compliance measured by equation (6).

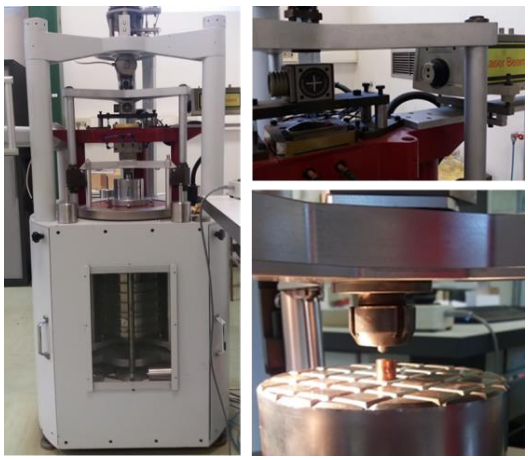

Figure 6. INRiM Primary Hardness Standard dead weight machine (details of the interferometric system and the anvil).

The micro-mechanical system, the optical microscopy imaging technique (INRiM patent), and the image processing technique used for the measurement of the indentation geometry are shown in Figure 7.

5. MATERIALS

The materials tested in this work are copper alloy, aluminum alloy, stainless steel, and brass. Young's modulus E and Poisson ratio ν_s of the tested materials were previously determined on the basis of accurate measurements of longitudinal c_l and transversal c_t sound speed waves in solids [19], at room temperature. Although some systematic differences between dynamic and static moduli can be achieved, the reference data can be considered sufficiently accurate and useful for the proposed comparison method, since overall uncertainties are lower than 1 %. In Table 1, the reference data of tested alloys are shown.

The dynamic Poisson ratio ν_s is calculated by means of the following equation:

$$\nu_s = \frac{1-2\left(\frac{c_l}{c_t}\right)^2}{2-2\left(\frac{c_l}{c_t}\right)^2} \tag{11}$$

the values of Poisson ratio ν_s, listed in Table 1 have been used in equation (1) for the indentation modulus calculation.

Dynamic Young's modulus E is calculated by means of the following equation:

$$E = 2\rho c_l^2(1-\nu_s) \tag{12}$$

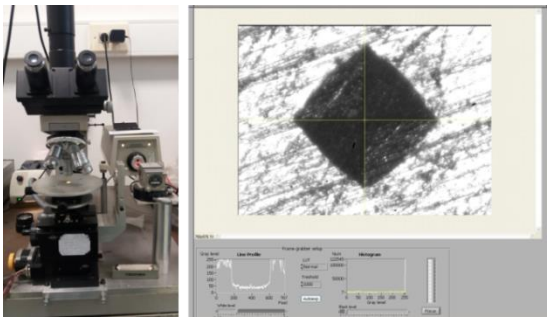

Figure 7: Optical microscopy system and imaging techniques for measuring geometrical dimensions of the indentations.

Table 1. Reference data on the tested metal alloys.

Parameter		Stainless steel	Aluminum alloy	Copper alloy	Brass
Density	ρ/kgm^{-3}	7914.1	2806.4	8932.5	8296.1
Longitudinal speed wave	c_l/ms^{-1}	5759.1	6294.7	4779.0	4520.3
Transversal speed wave	c_t/ms^{-1}	3146.2	3082.4	2247.8	1842.1
Young's modulus	E/GPa	201.7	71.6	122.6	78.9
Poisson's ratio	ν_s/–	0.287	0.342	0.358	0.400

6. EXPERIMENTAL RESULTS

In order to define the indentation modulus E_{IT}, Vickers hardness measurements are performed with maximum forces F_{MAX} of 980.6 N, 294.2 N, and 29.4 N. The Brinell hardness measurements, with maximum forces of 1838.6 N, 612.9 N, and 305.9 N, are performed by using the spherical indenter of radius R = 1.25 mm and 294.2 N, 98.1 N, and 49.0 N, by using the spherical indenter of radius R = 0.5 mm. The Young's modulus and Poisson ratio of the Vickers diamond pyramidal indenter are E_i = 1140 GPa and ν_i = 0.07 [1] respectively and the same values for the Brinell tungsten carbide spherical indenter are E_i = 634 GPa and ν_i = 0.22 respectively [20]. The values of the Young's modulus and Poisson ratio of the spherical indenter refer to the specific tungsten carbide-cobalt alloy (composition WC 94%/Co 6%), density 14800 kg/m^3 (ISO code K10, ANSI code C3).

The maximum indentation depth h_{MAX} is measured by means of the laser interferometric system and h_v from the hardness indentation, based on equation (7) and equation (9). Values of frame compliance C_f, are calculated by equation (6), and contact area A_p and sample compliance C_s are collected for each single measurement. The value of contact stiffness $S = \partial F / \partial h$, is calculated based on the Doerner-Nix linear model. Indentation hardness H_{IT} is determined, as stated in ISO 14577-1 [1], from the following equation: $H_{IT} = F_{MAX} / A_p$, where the contact area is expressed as a function of contact depth h_c, equation (4).

In the graphs shown in Figure 8, Figure 9, and Figure 10, the values of the maximum indentation depth h_{MAX} measured as a function of the maximum applied load F_{MAX} are depicted. In Figure 8, the values are determined based on the Vickers method, and in Figure 9 and Figure 10 the values are measured by means of the Brinell method, with both spherical indenter radii being 0.5 mm and 1.25 mm.

In the following Tables, all the experimental average values and empirical data of four metallic samples, used in equation (1) for model implementation, are collected.

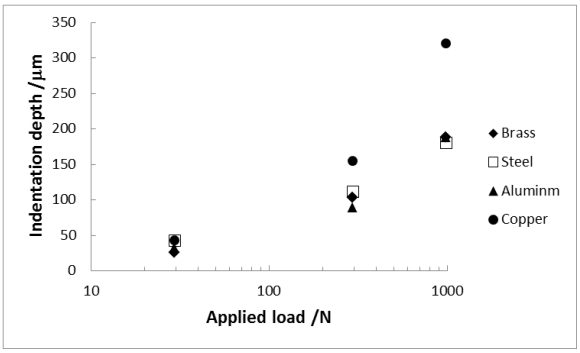

Figure 8: Experimental data of maximum indentation depth, measured from Vickers method, as a function of applied load.

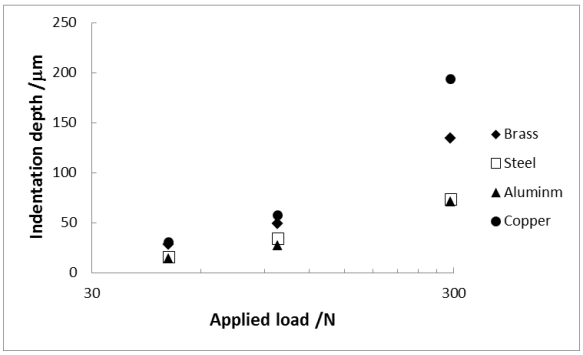

Figure 9: Experimental data of maximum indentation depth, measured from Brinell method (R = 0.5 mm), as a function of applied load.

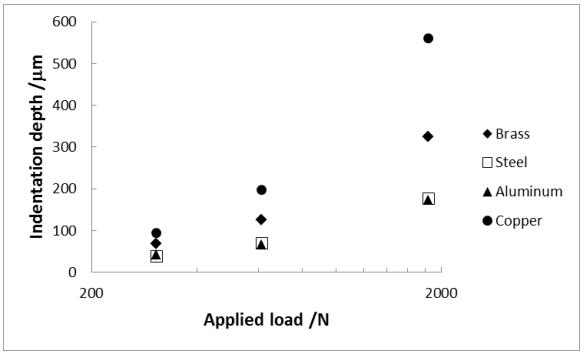

Figure 10: Experimental data of maximum indentation depth, measured from Brinell method (R = 1.25 mm), as a function of applied load.

Table 2. Vickers hardness test: data on brass.

Experimental data		HV3	HV30	HV100
Maximum applied load	F_{MAX}/N	29.4	294.2	980.6
Maximum indentation depth	h_{MAX}/μm	32.5	103.0	187.8
Maximum indentation depth	h_v/μm	227.1	719.2	1311.6
Square impression side	l/μm	160.6	508.5	927.4
Contact area	A_p/m	$1.47 \cdot 10^{-8}$	$2.39 \cdot 10^{-7}$	$7.79 \cdot 10^{-7}$
Sample compliance	C_s/mN^{-1}	$2.63 \cdot 10^{-12}$	$3.79 \cdot 10^{-13}$	$1.30 \cdot 10^{-13}$
Hardness	H_{IT} /GPa	199.8	122.9	125.9
Frame compliance	C_f / mN^{-1}	(-2.26E^{-07})	$2.49 \cdot 10^{-9}$	$6.92 \cdot 10^{-10}$
Contact stiffness	S/ Nm^{-1}	$1.62 \cdot 10^{7}$	$4.51 \cdot 10^{7}$	$7.21 \cdot 10^{7}$
Indentation Modulus	E_{IT}/ GPa	85.3	74.7	65.4

Table 3. Vickers hardness test: data on stainless steel.

Experimental data		HV3	HV30	HV100
Maximum applied load	F_{MAX}/N	29.4	294.2	980.6
Maximum indentation depth	h_{MAX}/μm	43.5	112.1	181.0
Maximum indentation depth	h_v/μm	23.2	80.1	147.8
Square impression side	l/μm	114.8	395.7	729.9
Contact area	A_p/m	$4.38 \cdot 10^{-8}$	$2.83 \cdot 10^{-7}$	$7.19 \cdot 10^{-7}$
Sample compliance	C_s/mN^{-1}	$5.74 \cdot 10^{-12}$	$5.08 \cdot 10^{-13}$	$1.51 \cdot 10^{-13}$
Hardness	H_{IT} /GPa	67.1	104.0	136.4
Frame compliance	C_f / mN^{-1}	($6.89 \cdot 10^{-7}$)	$1.09 \cdot 10^{-7}$	$3.38 \cdot 10^{-8}$
Contact stiffness	S/ Nm^{-1}	$1.80 \cdot 10^{7}$	$4.75 \cdot 10^{7}$	$7.56 \cdot 10^{7}$
Indentation Modulus	E_{IT}/ GPa	154.5	114.8	98.6

Table 4. Vickers hardness test: data on aluminum alloy.

Experimental data		HV3	HV30	HV100
Maximum applied load	F_{MAX}/N	29.4	294.2	980.6
Maximum indentation depth	h_{MAX}/μm	32.0	89.6	187.7
Maximum indentation depth	h_v/μm	25.4	80.9	149.1
Square impression side	l/μm	125.4	399.6	736.4
Contact area	A_p/m	$2.16 \cdot 10^{-8}$	$1.64 \cdot 10^{-7}$	$7.27 \cdot 10^{-7}$
Sample compliance	C_s/mN^{-1}	$7.12 \cdot 10^{-12}$	$6.36 \cdot 10^{-13}$	$2.39 \cdot 10^{-13}$
Hardness	H_{IT} /GPa	136.4	179.1	134.9
Frame compliance	C_f / mN^{-1}	($2.26 \cdot 10^{-7}$)	$2.95 \cdot 10^{-8}$	$3.94 \cdot 10^{-8}$
Contact stiffness	S/ Nm^{-1}	$9.32 \cdot 10^{6}$	$2.86 \cdot 10^{7}$	$4.75 \cdot 10^{7}$
Indentation Modulus	E_{IT}/ GPa	68.5	66.0	59.7

Table 5. Vickers hardness test: data on copper alloy.

Experimental data		HV3	HV30	HV100
Maximum applied load	F_{MAX}/N	29.4	294.2	980.6
Maximum indentation depth	h_{MAX}/μm	43.6	155.3	320.4
Maximum indentation depth	h_v/μm	41.7	151.9	293.3
Square impression side	l/μm	206.0	749.8	1448.1
Contact area	A_p/m	$4.44 \cdot 10^{-8}$	$5.64 \cdot 10^{-7}$	$2.39 \cdot 10^{-6}$
Sample compliance	C_s/mN^{-1}	$2.69 \cdot 10^{-12}$	$2.92 \cdot 10^{-13}$	$1.15 \cdot 10^{-13}$
Hardness	H_{IT} /GPa	66.3	52.2	41.0
Frame compliance	C_f / mN^{-1}	($6.31 \cdot 10^{-8}$)	$1.16 \cdot 10^{-8}$	$2.77 \cdot 10^{-8}$
Contact stiffness	S/ Nm^{-1}	$2.15 \cdot 10^{7}$	$6.15 \cdot 10^{7}$	$9.14 \cdot 10^{7}$
Indentation Modulus	E_{IT}/ GPa	90.2	69.4	52.8

Table 6. Brinell hardness test: data on brass.

Experimental data		HBW (5) R=0.5	HBW (10) R=0.5	HBW (30) R=0.5	HBW (31.2) R=1.25	HBW (62.5) R=1.25	HBW (187.5) R=1.25
Maximum applied load	F_{MAX}/N	49.0	98.1	294.2	305.9	612.8	1838.6
Maximum indentation depth	h_{MAX}/μm	28.3	49.4	134.5	69.0	125.7	323.7
Maximum indentation depth	h_v/μm	24.7	45.7	123.3	63.8	115.4	306.1
Radius of the impression	r/μm	155.3	208.8	328.8	394.2	524.7	819.5
Contact area	A_p/m²	$8.02\cdot10^{-8}$	$1.37\cdot10^{-7}$	$3.48\cdot10^{-7}$	$4.88\cdot10^{-7}$	$8.75\cdot10^{-7}$	$2.09\cdot10^{-6}$
Sample compliance	C_s/mN^{-1}	$2.64\cdot10^{-12}$	$1.61\cdot10^{-12}$	$6.11\cdot10^{-13}$	$4.15\cdot10^{-13}$	$2.45\cdot10^{-13}$	$1.02\cdot10^{-13}$
Hardness	H_{IT} /GPa	61.1	71.6	84.5	62.6	70.0	87.7
Frame compliance	C_f / mN^{-1}	$7.36\cdot10^{-8}$	$3.81\cdot10^{-8}$	$3.82\cdot10^{-8}$	$1.71\cdot10^{-8}$	$1.67\cdot10^{-8}$	$9.59\cdot10^{-9}$
Contact stiffness	S/ Nm^{-1}	$1.75\cdot10^{7}$	$1.97\cdot10^{7}$	$2.88\cdot10^{7}$	$4.33\cdot10^{7}$	$5.17\cdot10^{7}$	$6.84\cdot10^{7}$
Indentation Modulus	E_{IT}/ GPa	54.1	46.0	42.0	54.2	47.9	40.4

Table 7. Brinell hardness test: data on stainless steel.

Experimental data		HBW (5) R=0.5	HBW (10) R=0.5	HBW (30) R=0.5	HBW (31.2) R=1.25	HBW (62.5) R=1.25	HBW (187.5) R=1.25
Maximum applied load	F_{MAX}/N	49.0	98.1	294.2	305.9	612.8	1838.6
Maximum indentation depth	h_{MAX}/μm	16.5	34.5	73.9	39.3	71.0	177.6
Maximum indentation depth	h_v/μm	10.0	19.6	56.7	28.0	51.9	136.2
Radius of the impression	r/μm	99.5	138.5	231.2	263.5	356.7	567.5
Contact area	A_p/m²	$4.34\cdot10^{-8}$	$9.36\cdot10^{-8}$	$1.94\cdot10^{-7}$	$2.62\cdot10^{-7}$	$4.75\cdot10^{-7}$	$1.15\cdot10^{-6}$
Sample compliance	C_s/mN^{-1}	$3.64\cdot10^{-12}$	$2.02\cdot10^{-12}$	$6.98\cdot10^{-13}$	$4.79\cdot10^{-13}$	$2.73\cdot10^{-13}$	$1.18\cdot10^{-13}$
Hardness	H_{IT} /GPa	112.8	104.7	152.0	116.6	128.9	159.5
Frame compliance	C_f / mN^{-1}	$1.33\cdot10^{-7}$	$1.52\cdot10^{-7}$	$5.85\cdot10^{-8}$	$3.69\cdot10^{-8}$	$3.11\cdot10^{-8}$	$2.25\cdot10^{-8}$
Contact stiffness	S/ Nm^{-1}	$1.47\cdot10^{7}$	$1.96\cdot10^{7}$	$2.78\cdot10^{7}$	$4.15\cdot10^{7}$	$5.09\cdot10^{7}$	$6.53\cdot10^{7}$
Indentation Modulus	E_{IT}/ GPa	62.5	56.3	55.3	72.9	65.7	53.0

Table 8. Brinell hardness test: data on aluminum alloy.

Experimental data		HBW (5) R=0.5	HBW (10) R=0.5	HBW (30) R=0.5	HBW (31.2) R=1.25	HBW (62.5) R=1.25	HBW (187.5) R=1.25
Maximum applied load	F_{MAX}/N	49.0	98.1	294.2	305.9	612.8	1838.6
Maximum indentation depth	h_{MAX}/μm	14.9	27.8	71.4	41.8	66.6	174.1
Maximum indentation depth	h_v/μm	11.3	19.0	53.5	25.7	47.6	138.6
Radius of the impression	r/μm	105.5	136.5	225	252.5	341.7	572.2
Contact area	A_p/m²	$3.29\cdot10^{-8}$	$6.55\cdot10^{-8}$	$1.72\cdot10^{-7}$	$2.41\cdot10^{-7}$	$3.94\cdot10^{-7}$	$1.07\cdot10^{-6}$
Sample compliance	C_s/mN^{-1}	$5.22\cdot10^{-12}$	$2.96\cdot10^{-12}$	$1.13\cdot10^{-12}$	$9.38\cdot10^{-13}$	$4.45\cdot10^{-13}$	$1.56\cdot10^{-13}$
Hardness	H_{IT} /GPa	149.2	149.6	170.6	127.2	155.6	171.2
Frame compliance	C_f / mN^{-1}	$7.5\cdot10^{-8}$	$8.93\cdot10^{-8}$	$6.1\cdot10^{-8}$	$5.24\cdot10^{-8}$	$3.1\cdot10^{-8}$	$1.93\cdot10^{-8}$
Contact stiffness	S/ Nm^{-1}	$0.84\cdot10^{7}$	$1.14\cdot10^{7}$	$1.67\cdot10^{7}$	$2.52\cdot10^{7}$	$2.97\cdot10^{7}$	$4.74\cdot10^{7}$
Indentation Modulus	E_{IT}/ GPa	39.7	38.0	34.2	43.0	40.5	39.0

Table 9. Brinell hardness test: data on copper alloy.

Experimental data		HBW (5) R=0.5	HBW (10) R=0.5	HBW (30) R=0.5	HBW (31.2) R=1.25	HBW (62.5) R=1.25	HBW (187.5) R=1.25
Maximum applied load	F_{MAX}/N	49.0	98.1	294.2	305.9	612.8	1838.6
Maximum indentation depth	h_{MAX}/μm	30.7	57.9	193.3	93.2	196.6	561.5
Maximum indentation depth	h_v/μm	25.0	50.3	168.2	77.2	158.1	468.3
Radius of the impression	r/μm	156	218.5	374	432.7	608.5	975.5
Contact area	A_p/m²	$8.74\cdot10^{-8}$	$1.62\cdot10^{-7}$	$4.78\cdot10^{-7}$	$6.7\cdot10^{-7}$	$1.37\cdot10^{-6}$	$3.34\cdot10^{-6}$
Sample compliance	C_s/mN^{-1}	$2.67\cdot10^{-12}$	$1.45\cdot10^{-12}$	$5.12\cdot10^{-13}$	$4.01\cdot10^{-13}$	$2.27\cdot10^{-13}$	$8.9\cdot10^{-14}$
Hardness	H_{IT} /GPa	56.1	60.3	61.6	45.6	44.6	54.9
Frame compliance	C_f / mN^{-1}	$1.16\cdot10^{-7}$	$7.83\cdot10^{-8}$	$8.56\cdot10^{-8}$	$5.2\cdot10^{-8}$	$6.28\cdot10^{-8}$	$5.06\cdot10^{-8}$
Contact stiffness	S/ Nm^{-1}	$1.80\cdot10^{7}$	$2.25\cdot10^{7}$	$3.45\cdot10^{7}$	$4.78\cdot10^{7}$	$5.98\cdot10^{7}$	$7.98\cdot10^{7}$
Indentation Modulus	E_{IT}/ GPa	53.2	48.5	43.0	50.8	43.9	37.1

7. EVALUATION OF INDENTATION MODULUS E_{IT}

As is evident from the experimental data summarized in Tables 2-9, all the data shows a systematic dependence as a function of applied load. In general terms, the data suggests that evaluations of an indentation modulus at lower values of applied load ($F_{MAX} < 100$ N) are less accurate than other values, for both the Vickers and Brinell methods, at the macro-scale level. The uncertainty is due to the determination of contact stiffness S. In fact, estimation of the unloading indentation slope is less accurate for low values of applied force (since the indentation depth is small) than indentation curves of greater indentation depth. Consequently, the number of points of the curve on which the regression is applied is exiguous for low indentation depth. For example, in Figure 11, a comparison between the Doener-Nix model and the actual best fit of the unloading curve returns two different slopes of about 2.5%, from which contact stiffness S is evaluated.

As is evident from the diagram, by applying the Doener-Nix method to the raw data (taking into account the initial 20% of the unloading curve), the resultant contact stiffness is $S = 18.05 \cdot 10^6$ N m^{-1} (as shown in Table 9), while if the actual best fit is applied, the resultant contact stiffness is $S = 18.51 \cdot 10^6$ N m^{-1}. This difference (of only 2.5%) results in a difference in the indentation modulus of about 5% or more.

Moreover, the effects of frame compliance are relevant to the low values of indentation depth [21]. Nevertheless, it is known that the poorly defined tip shape of the Vickers indenters at low indentation depths is a cause of hardness measurement errors [22]. On the other hand, the piling-up effects in the Brinell tests, at low values of indentation depth ($h_{MAX} < 50$ μm), allow for evaluations of the geometrical dimensions of the spherical impression to be less accurate than the impressions affected by the sinking-in effects as well as the indentation size effects [23]. More in-depth analyses are currently underway, considering the validity of the assumption of a load-independent value for C_f and further checking the homogeneity of the tested materials.

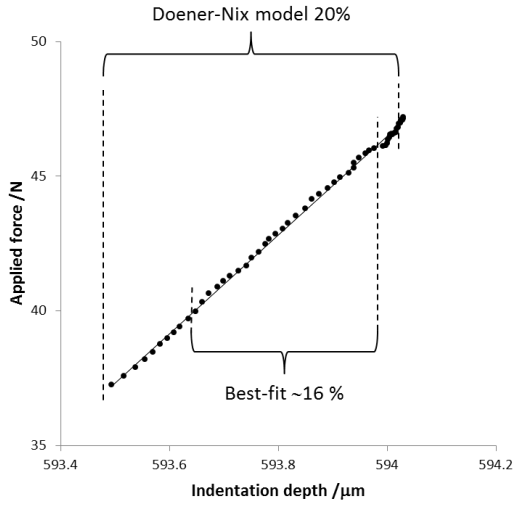

Figure 11: Determination of contact stiffness on the basis of the Doener-Nix method and from the actual best fit of the unloading curve (for copper, HBW (5), R=0.5mm).

In the graphs shown in Figure 12, Figure 13, and Figure 14, the indentation modulus E_{IT} (with the related expanded uncertainties) of the tested materials is demonstrated. In the graph in Figure 12, the indentation modulus is determined on the basis of the Vickers method, and in Figure 13 and Figure 14, it is determined on the basis of the Brinell method. The indentation modulus is expressed as a function of applied load.

In the following graphs shown in Figure 15, Figure 16, Figure 17, and Figure 18, the average indentation modulus E_{IT} of each sample is compared with Young's modulus E. Values for the indentation modulus are determined by the data shown above on the basis of equation (1). Data on the Young's modulus is evaluated on the basis of equation (11) and equation (12), based on measurements of the speed of sound in solids. The observed load dependence of all experimental data allows for the achievement of a relevant load-dependent indentation modulus.

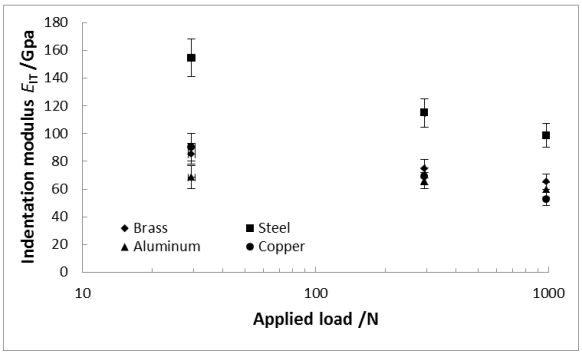

Figure 12: Indentation modulus calculated using the Vickers method.

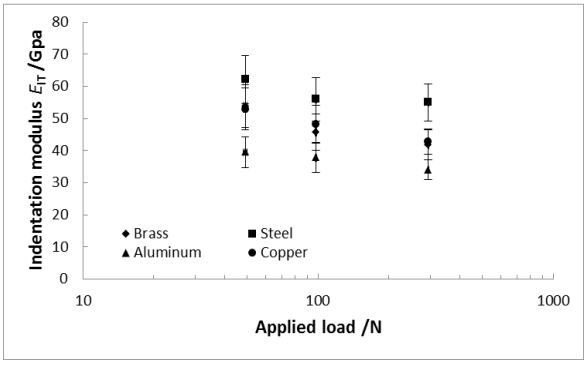

Figure 13: Indentation modulus from Brinell method (R=0.5 mm).

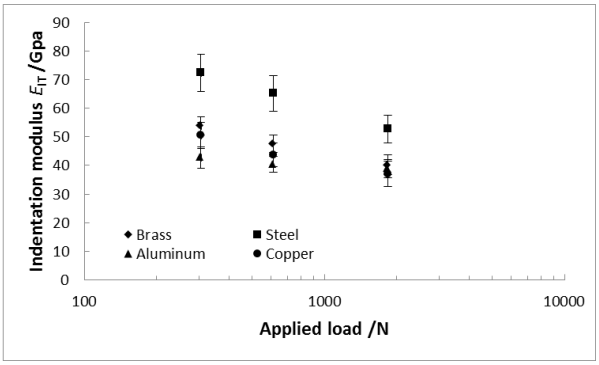

Figure 14: Indentation modulus calculated using the Brinell method (R=1.25

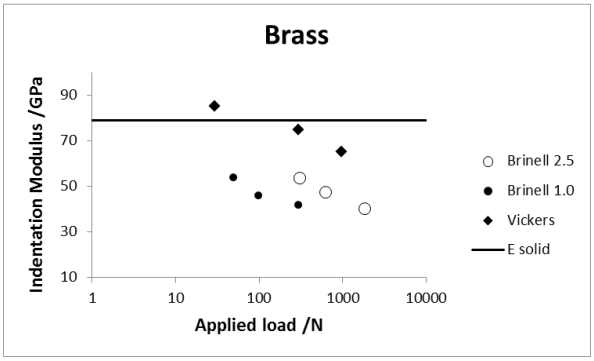

Figure 15: Indentation modulus and Young's modulus for brass.

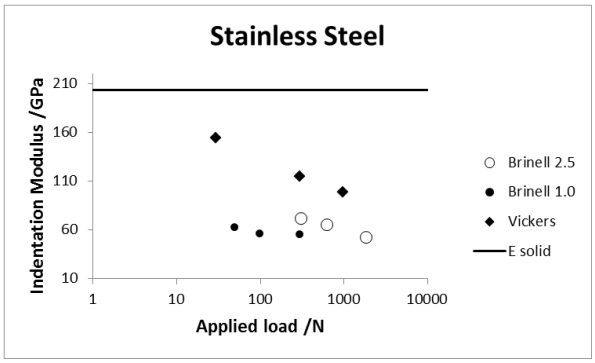

Figure 16: Indentation modulus and Young's modulus for stainless steel.

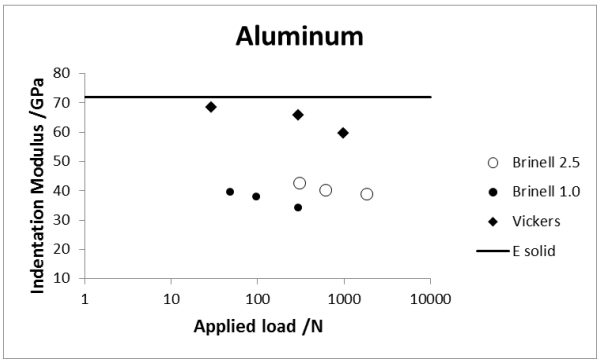

Figure 17: Indentation modulus and Young's modulus for aluminum.

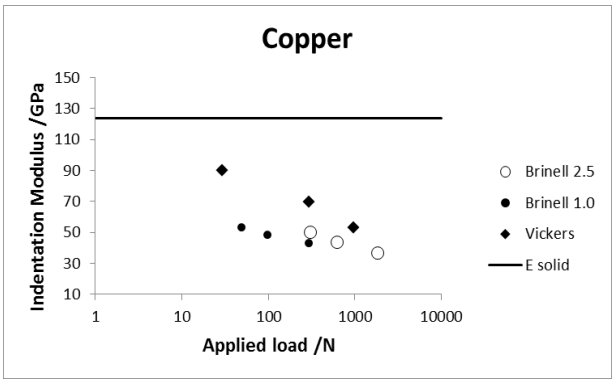

Figure 18: Indentation modulus and Young's modulus for brass.

8. CONCLUSION

This paper has described a method for the evaluation of the indentation modulus by using the primary hardness standard machine at INRiM in the macro-scale range, with both Vickers and Brinell indenters. The indentation modulus is calculated based on the Doerner-Nix linear model and from accurate measurements of indentation load, indentation depth, and projected contact area. Vickers and Brinell hardness impression imaging methods were measured by means of optical microscopy imaging techniques. In particular, a detailed analysis of frame compliance was performed and discussed. Preliminary tests were performed on brass, stainless steel, aluminum alloy, and copper alloy samples and experimental data and results were presented.

The primary finding of this study is that the indentation modulus at a macro-scale level is strongly load/indentation depth-dependent. Large plastic effects occurring at high values of applied load affect the evaluation of the indentation modulus, since the method is based on the determination of the elastic response of the material under investigation. Consequently, the indentation modulus is greatly underestimated with respect to Young's modulus. On the contrary, at lower values of applied load, values of indentation modulus tend to increase, since elastic behavior tends to be predominant with respect to the plastic behavior.

ACKNOWLEDGEMENT

The research leading to these results was conducted in the frame of EMPIR 14IND03 "Strength-ABLE". The EMPIR is jointly funded by the EMPIR participating countries within EURAMET and the European Union.

REFERENCES

[1] ISO 14577-11:2002. Metallic materials: Instrumented indentation test for hardness and materials parameters Part 1: test method.

[2] N. A. Stilwell, D. Tabor, Elastic recovery of conical indentations. Proc. of the Physical Society 78, 2 (1961) pp. 169-179.

[3] J. B. Pethicai, R. Hutchings, W. C. Oliver, Hardness measurement at penetration depths as small as 20 nm. Philosophical magazine 48, 4 (1983) pp. 593-606.

[4] M. F. Doerner, W. D. Nix, A method for interpreting the data depth-sensing indentation instruments. J. Mater. Res 1, 4 (1986) pp. 601-609.

[5] W. C. Oliver, G. M. Pharr, An improved technique for determining hardness and elastic modulus using load and displacement sensing indentation experiments. Journal of Materials Research 7, 6 (1992) pp. 1564-1583.

[6] Y.W. Bao, W. Wang, Y.C. Zhou, Investigation of the relationship between elastic modulus and hardness based on depth-sensing indentation measurements. Acta Materialia 52 (2004) pp. 5397–5404.

[7] J. E. Zorzi, C.A. Perottoni, Estimating Young's modulus and Poisson's ratio by instrumented indentation test. Materials Science & Engineering A, 574 (2013) pp. 25-30.

[8] J. Prou, K. Kishimoto, A. Constantinescu, Identification of Young's Modulus from Indentation Testing and Inverse Analysis. Journal of Solid Mechanics and Materials Engineering 4, 6 (2010) pp. 781-795.

[9] T. Chudoba, N. M. Jennett, Higher accuracy analysis of instrumented indentation data obtained with pointed indenters. Journal of Physics D: Applied Physics 41, 21 (2008) p. 215407.

[10] C. Ullner, E. Reimann, H. Kohlhoff, A. Subaric-Leitis, Effect and measurement of the machine compliance in the macro range of the instrumented indentation test. Measurement 43, 2 (2010) pp. 216-222.
[11] R. Cagliero, G. Barbato, G. Maizza, G. Genta, Measurement of elastic modulus by instrumented indentation in the macro-range: Uncertainty evaluation. International Journal of Mechanical Sciences 101 (2015) pp. 161-169.
[12] A. Schiavi, C. Origlia, A. Germak, G. Barbato, G. Maizza, G. Genta, R. Cagliero, G. Coppola, "Measurement of macro-scale indentation modulus using the primary hardness standard machines at INRiM," Proc. of IMEKO TC3, TC5, and TC22 International Conference, 2017, Helsinki, Finland.
[13] K. Herrmann, N. M. Jennett, W. Wegener, J. Meneve, K. Hasche, R. Seemann, Progress in determination of the area function of indenters used for nanoindentation. Thin Solid Films 377-378 (2000) pp. 394-400.
[14] X. Hernot, O. Bartier, Y. Bekouche, R. El Abdi, G. Mauvoisin, Influence of penetration depth and mechanical properties on contact radius determination for spherical indentation. International Journal of Solids and Structures 43, 14-15 (2006), pp. 4136-4153.
[15] A. P. G. M Bolshakov, G. M. Pharr, Influences of pile-up on the measurement of mechanical properties by load and depth sensing indentation techniques. Journal of Materials Research 13, 4 (1998) pp. 1049-1058.
[16] G. Barbato, S. Desogus, R. Levi, Design and performance of a dead-weight standard Rockwell hardness testing machine. Journal of Testing and Evaluation 6 (1978) pp. 276-279.
[17] A. Germak, C. Origlia, Metrological characterization of the Vickers Hardness Calibration Machine and Gal-Vision measuring system realised By LTF for NIM (China). INRiM Tech. Report 16, 2006.
[18] A. Germak, A. Liguori, C. Origlia, "Experience in the metrological characterization of primary hardness standard machines," in Proc. of HARDMEKO, 2007.
[19] S. Lago, S. Brignolo, R. Cuccaro, C. Musacchio, P.G. Albo, P. Tarizzo, "Application of acoustic methods for a non-destructive evaluation of the elastic properties of several typologies of materials," Applied Acoustics 75 (2014), pp. 10-16.
[20] http://www.wesltd.com/divisions/hardmetal/html/Tungsten-carbide.html (last accessed 21/12/2018)
[21] A. Schiavi, C. Origlia, A. Cackett, C. Hardie, D. Signore, O. Petrella, A. Germak, Comparison between tensile properties and indentation properties measured with various shapes indenters of Copper-Chromium-Zirconium alloy at macroscale level. Journal of Physics: Conference Series 1065, 6 (2018) p. 062010.
[22] I. Spary, A. Bushby, N.M. Jennett., On the indentation size effect in spherical indentation. Philosophical Magazine 86, 33-35 (2006) pp. 5581-5593.
[23] A. J. Cackett, J. J. H. Lim, P. Klupś, A. J. Bushby, C. D. Hardie, Using spherical indentation to measure the strength of copper-chromium-zirconium. Journal of Nuclear Materials (2018) pp. 1-7.